A Spontaneous Nonhuman Primate Model of Myopic Foveoschisis

Tzu-Ni Sin,[1] Sangbae Kim,[2] Yumei Li,[2] Jun Wang,[2] Rui Chen,[2] Sook Hyun Chung,[1] Soohyun Kim,[1,5] M. Isabel Casanova,[1,5] Sangwan Park,[1,5] Zeljka Smit-McBride,[1] Ning Sun,[1] Ori Pomerantz,[3] Jeffrey A. Roberts,[3] Bin Guan,[4] Robert B. Hufnagel,[4] Ala Moshiri,[1] Sara M. Thomasy,[1,5] Paul A. Sieving,[1] and Glenn Yiu[1]

[1]Department of Ophthalmology & Vision Science, University of California Davis, Davis, California, United States
[2]Department of Molecular and Human Genetics, Baylor College of Medicine, Houston, Texas, United States
[3]California National Primate Research Center, Davis, California, United States
[4]Ophthalmic Genetics and Visual Function Branch, National Eye Institute, National Institutes of Health, Bethesda, Maryland, United States
[5]Department of Surgical & Radiological Sciences, University of California Davis, Davis, California, United States

Correspondence: Glenn Yiu, Department of Ophthalmology & Vision Science, University of California, Davis, 4860 Y St., Suite 2400, Sacramento, 95817 CA, USA; gyiu@ucdavis.edu.

Received: October 20, 2022
Accepted: January 5, 2023
Published: January 23, 2023

Citation: Sin TN, Kim S, Li Y, et al. A spontaneous nonhuman primate model of myopic foveoschisis. *Invest Ophthalmol Vis Sci.* 2023;64(1):18. https://doi.org/10.1167/iovs.64.1.18

Purpose. Foveoschisis involves the pathologic splitting of retinal layers at the fovea, which may occur congenitally in X-linked retinoschisis (XLRS) or as an acquired complication of myopia. XLRS is attributed to functional loss of the retinal adhesion protein retinoschisin 1 (RS1), but the pathophysiology of myopic foveoschisis is unclear due to the lack of animal models. Here, we characterized a novel nonhuman primate model of myopic foveoschisis through clinical examination and multimodal imaging followed by morphologic, cellular, and transcriptional profiling of retinal tissues and genetic analysis.

Methods. We identified a rhesus macaque with behavioral and anatomic features of myopic foveoschisis, and monitored disease progression over 14 months by fundus photography, fluorescein angiography, and optical coherence tomography (OCT). After necropsy, we evaluated anatomic and cellular changes by immunohistochemistry and transcriptomic changes using single-nuclei RNA-sequencing (snRNA-seq). Finally, we performed Sanger and whole exome sequencing with focus on the *RS1* gene.

Results. Affected eyes demonstrated posterior hyaloid traction and progressive splitting of the outer plexiform layer on OCT. Immunohistochemistry showed increased GFAP expression in Müller glia and loss of ramified Iba-1+ microglia, suggesting macro- and microglial activation with minimal photoreceptor alterations. SnRNA-seq revealed gene expression changes predominantly in cones and retinal ganglion cells involving chromatin modification, suggestive of cellular stress at the fovea. No defects in the *RS1* gene or its expression were detected.

Conclusions. This nonhuman primate model of foveoschisis reveals insights into how acquired myopic traction leads to phenotypically similar morphologic and cellular changes as congenital XLRS without alterations in RS1.

Keywords: myopia, myopic foveoschisis, nonhuman primate, x-linked retinoschisis (XLRS), animal model

Foveoschisis is an ocular condition that is characterized by schisis, or separation, of the neurosensory retina into two or more layers at the fovea – the specialized, cone-rich central region of the macula that is required for high-acuity vision in simian primates.[1] A congenital form of macular schisis occurs in predominantly men due to its X-linked inheritance,[2] and has been attributed to functional loss of the *retinoschisin 1* (*RS1*) gene product.[3] Female carriers are often asymptomatic, although rare cases of women with X-linked retinoschisis (XLRS) phenotypes have also been documented.[4] Patients with XLRS develop vision loss at a young age, often before their teenage years,[3,5] and may progress slowly with time. The classical clinical appearance involves macular schisis with a "spokewheel" pattern radiating from the fovea, whereas some patients may also develop macular atrophy that results in worsened vision. Electroretinography (ERG) shows a reduced bipolar b-wave compared to photoreceptor a-wave due to disruption in synaptic transmission between photoreceptors and ON-bipolar cells. Expressed in bipolar and photoreceptor cells, the RS1 protein is released into the extracellular matrix to mediate cell-to-cell adhesion and signal transduction through attachments to the photoreceptor inner segments and bipolar cells.[3,6,7] Mutant mice lacking the murine *RS1* gene exhibit intraretinal schisis, reactive gliosis, and reduced ERG b-wave to a-wave amplitude ratio similar to patients with XLRS.[8] An Rs1h$^{-/y}$ knockout rat model has also been generated, which exhibits schisis cavities at

postnatal day 15 and photoreceptor cell damage starting at p21. Although no treatments are currently available, gene therapy by intravitreal injection of adeno-associated virus (AAV8-*RS1*) in patients with XLRS is undergoing clinical evaluation in humans (ClinicalTrials.gov: NCT02317887).

An acquired form of foveoschisis may also occur in patients with high or pathologic myopia, and is a major cause of visual loss in patients with myopia.[9] Optical coherence tomography (OCT) imaging, which provides noninvasive, near-histologic visualization of retinal layers,[10–12] demonstrates schisis cavities most often at the outer plexiform layer (OPL),[13] although separation may also occur at the internal limiting membrane (ILM), inner segment/outer segment (IS/OS) junction, retinal pigment epithelium (RPE), or a combination of different layers.[14–16] Myopic foveoschisis is attributed to the inward tension and mechanical strain on the inner retina as a result of axial elongation of the eye wall in patients with high myopia.[1] Management of this condition is generally surgical, and involves the use of vitrectomy with or without ILM peeling and gas tamponade in patients experiencing visual decline.[17,18] Because myopic foveoschisis is initially asymptomatic and progresses slowly, the condition may be underdiagnosed and is difficult to treat.

Although the pathophysiology of XLRS has been extensively characterized, little is known about the development of myopic foveoschisis at a cellular, molecular, or genetic level, due to the rarity of animal models of myopia in species that possess a fovea. Experimental myopia can be induced by spectacle lens compensation or form deprivation by lid suturing in mice, chickens, guinea pigs, and tree shrews, but these animal models do not reflect the natural process of myopia development in humans and do not result in foveoschisis.[19] Nonhuman primates (NHPs) possess a macula resembling those in humans, but studies of experimental myopia in these animals focus on eye growth during infancy, and potential benefits from refractive, surgical, or pharmacologic interventions,[20–22] rather than the pathologic impact of long-term degenerative myopia on the retina. In this study, we report and characterize a rhesus macaque (*Macaca mulatta*) which exhibited visual behavior of severe myopia, axial elongation, and anatomic features of myopic foveoschisis in both eyes. We characterized the condition's progression by clinical examination and in vivo imaging, then analyzed the morphologic, cellular, and gene expression profile of retinal tissues from this animal compared with age-matched control animals. Finally, we compared our findings about myopic foveoschisis to what is known about XLRS, providing new insights into the cellular and molecular mechanisms that may be common between these phenotypically similar, but mechanistically distinct pathologic entities.

Methods

Clinical Examination

Adult rhesus macaques, including the affected and normal control animals, underwent complete ophthalmic examination after sedation with intramuscular ketamine hydrochloride, midazolam, and dexmedetomidine, and pupil dilation using phenylephrine (Paragon), tropicamide (Bausch & Lomb), and cyclopentolate (Akorn). Cycloplegic streak retinoscopy was performed by a board-certified veterinary ophthalmologist (author S.T.). External photographs were captured using a digital single-lens reflex camera (Rebel T3; Canon). Anterior segment examinations were performed using a portable slit lamp (SL-7E; Topcon), and retinal fundus examinations were conducted using an indirect ophthalmoscope (Heine). Intraocular pressures (IOPs) were measured by rebound tonometry (TA01i; Icare). Axial length, vitreous length, anterior chamber (AC) depth, and lens thickness were measured using A-scan biometry (Sonomed Pacscan Plus; Escalon).

Multimodal Ocular Imaging

For imaging rhesus macaques, color fundus photography was performed using the CF-1 Retinal Camera (Canon) with a 50-degree wide-angle lens. Near infrared reflectance (IR), fluorescein angiography (FA), blue-peak fundus autofluorescence (AF), and spectral domain OCT imaging were performed using the Spectralis HRA + OCT system (Heidelberg Engineering) using a 30-degree or 55-degree objective. Confocal scanning laser ophthalmoscopy (SLO) was used to capture IR images at 815 nm, and FA/AF images at 488 nm excitation. For FA, animals were injected intravenously with 7.7 mg/kg fluorescein sodium (Akorn), and serial images were captured up to 15 minutes after dye injection. Spectral domain OCT images were captured as a 20 × 20–degree volume scan and a 30 × 5–degree raster scan protocol, centered on the fovea, with progression mode and retinal vessel tracking enabled to reliably image the same area longitudinally. Clinical OCT imaging of human patients were captured using the same imaging platform and protocol at the UC Davis Eye Center retina clinic. All SLO and OCT mages were analyzed using the Heidelberg Explorer software (version 1.9.13.0; Heidelberg Engineering).

Tissue Embedding and Immunohistochemistry

For immunohistochemistry, entire globes were enucleated at necropsy and immediately placed in 4% paraformaldehyde. After removing the anterior segment by dissecting along the limbus to remove the cornea, lens, and vitreous body, the posterior eye cup was fixed with 4% paraformaldehyde for 2 hours at room temperature then rinsed with phosphate-buffered saline (PBS). The tissue was cryoprotected with 30% sucrose in PBS overnight, then embedded in optimal cutting temperature medium and cryosectioned at 18 µm using a cryostat (CM3050 S; Leica). For immunohistochemistry, sections were washed with PBS, blocked with 10% normal donkey serum for 30 minutes, then incubated in primary antibody for 1 to 2 hours at room temperature, followed by Alexa Fluor 488, 568, or 647-conjugated secondary antibodies for 1 additional hour at room temperature. Primary antibodies against glial fibrillary acidic protein/GFAP (1:200; Z0334; Dako), ionized calcium-binding adaptor-1/IBA-1 (1:100; AB10558; Wako), rhodopsin (1:100; MABN15; Millipore), and M/L opsin (1:200; AB4505; Millipore) were used. For detecting RS1 protein, cryosections were blocked with 5% normal goat serum and incubated with rabbit anti-RS1 for 2 hours at room temperature, followed by 3 times wash using PBS with 0.5% Triton X-100, followed by Alexa Fluor 555-conjugated secondary antibodies (Invitrogen) for 1 hour at room temperature. The RS1 antibody is a rabbit polyclonal antibody against amino acid residues 24 to 37 of the N-terminus of retinoschisin (1:1000, customized antibody; Thermo Fisher).[23](p3) Histo-

logical sections were imaged using a confocal microscope (FV3000; Olympus).

Single-Nuclei RNA Sequencing and Analysis

For single-nuclei RNA sequencing (snRNA-seq), entire globes enucleated at necropsy were stored in PBS. After removing the anterior segment as described above, radial cuts were created in the posterior eye cup to create 4 to 5 petals, and a 5-mm disposable biopsy punch (33–35, Integra Miltex) was used to create a macular punch centered at the fovea through the retinal tissue, which was placed immediately in liquid nitrogen for cryopreservation. Single-nuclei isolation and RNA sequencing were performed as previously described.[24] In brief, nuclei from the frozen retinal tissue were isolated using cold RNase-free lysis buffer (10 mM Tris-HCl, 10 mM NaCl, 3 mM $MgCl_2$, and 0.1% NP40), homogenized using a Wheaton Dounce Tissue Grinder, and centrifuged at 500 g to pellet the nuclei. The nuclei pellet was resuspended in fresh lysis buffer and homogenized to yield single-nuclei suspension. The snRNA-seq cDNA library preparation and sequencing were performed following manufacturer's protocols using the chromium single-cell 3′ reagent kit version 3 (10xgenomics.com). Sequencing was performed on the Illumina Novaseq 6000. Cell Ranger software version 3.1 (10xgenomics.com) with default settings was used for alignment, barcode assignment, and unique molecular identifier (UMI) counting of the raw sequencing data with Macaque reference Mmul-10 (https://useast.ensembl.org). After generating the UMI count profile, we applied Seurat 4.0 (https://satijalab.org/seurat) for quality control and downstream analysis. For quality control, we excluded genes detected in fewer than 3 cells, and cells were filtered out if UMI counts are less than the bottom 3% and greater than top 1% of total quantile. We removed cell-cycle effects by regressing out cell-cycle scores during data scaling using all signals associated with cell cycle with the "CellCycleScoring" function in Seurat. Next, a normalization method using the "SCTransform" function was used to normalize the gene expression matrix. For cell clustering, we selected variable genes and computed principal components for dimensional reduction of UMAP with default parameters in Seurat. Next, we performed clustering using "FindClusters" in Seurat to identify sub-cell-type clusters. The top 20 principal components were used with 0.1 resolution, and the subpopulations of retinal cells are visualized using UMAP. We then integrated data sets using canonical correlation analysis (CCA) in Seurat and identified the major retinal cell type of each cluster using known markers. To identify differentially expressed genes (DEGs) between the affected animal and three pooled controls for each cell type, we used the "FindAllMarkers" function based on the Wilcoxon rank sum test in Seurat with default parameters, and identified DEGs with a threshold for adjusted $P < 0.001$ and fold change (FC) >2. Finally, Gene Ontology (GO) of significant DEGs were analyzed using the clusterProfiler package in Bioconductor (https://bioconductor.org), and GO terms with adjusted $P < 0.001$ were considered statistically significant.

Sanger Sequencing

Blood samples were collected from the affected and control macaques for genomic DNA extraction and Sanger sequencing using standard methods. Briefly, genomic DNA was amplified by polymerase chain reaction (PCR) using the BigDye Direct PCR master mix (ThermoFisher) using the following program, 96°C for 5 minutes, 35 cycles of 94°C for 30 seconds, 55°C for 45 seconds, 68°C for 45 seconds, and the final extension at 72°C for 2 minutes. The primer sets for each of the 6 exons of the human *RS1* gene were used in the PCR as shown in the Supplementary Table S1. The *RS1* loci including introns in human (GRCh37/hg19) and rhesus (Mmul_10/rheMac10) genomes shared 93.2% sequence identity, and the PCR amplicons shared 93.1% to 96.5% sequence identity (see Supplementary Table S1). Sanger sequencing was performed using the BigDye Direct kit.

Whole Exome Sequencing

One ug genomic DNA was sheared for 70 seconds with Covaris and was purified with Ampure XP beads. Following end repair and A-tailing, indexed adaptors were added to the product. The product was purified with Ampure XP beads, and was amplified with KAPA HiFi HotStart ReadyMix. The library was processed with Nimblegen SeqCap EZ protocol (Roche) using Rhexome v2 capture reagent.[25] Briefly, the sample was hybridized to probe pool, and captured with Dyanbeads M270 Streptavidin. After wash, captured DNA was amplified with KAPA HiFi HotStart ReadyMix. After cleanup and quantification, the diluted library was sequenced in the Illumina Novaseq6000 Sequencer. The library kit is KAPA HyperPrep Kit (Roche).

Bioinformatics Analysis

The sequencing reads were aligned to the rhesus reference genome assembly (Mmul_10) with BWA mem. The single nucleotide variants (SNVs) and short insertion/deletions (indels) were called following the GATK pipeline. The variants were annotated with variant effect predictor (VEP) based on gene models of Mmul_10. The orthologous human positions were identified by lifting over the variants in rhesus genome position to the human genome (hg19). ANNOVAR (v. 07/17/2017)[26] and dbNSFP (v.3.5a, including PolyPhen-2, REVEL score, etc.)[27–30] were used to annotate and predict the protein-altering effects of the variants based on the gene model of hg19. CADD score was obtained from https://cadd.gs.washington.edu.[31] We then focused on the variants in the inherited retinal disease genes downloaded from https://sph.uth.edu/retnet/home.htm. Additionally, we checked the variants in the genes associated with familial exudative vitreoretinopathy[32] or Stickler syndrome (OMIM).

Study Approval

The California National Primate Center (CNPRC) is accredited by the Association for Assessment and Accreditation of Laboratory Animal Care (AAALAC) International. All studies using rhesus macaques (*Macaca mulatta*) followed the guidelines of the Association for Research in Vision and Ophthalmology (ARVO) Statement for the Use of Animals in Ophthalmic and Vision Research, and complied with the National Institutes of Health (NIH) Guide for the Care and Use of Laboratory Animals. All procedures were conducted under protocols approved by the University of California, Davis Institutional Animal Care and Use Committee (IACUC).

Investigative Ophthalmology & Visual Science

Results

Clinical Examination and Multimodal Imaging of NHP Foveoschisis

A 27-year-old male rhesus macaque was noted to exhibit visual behaviors of myopia by the behavioral staff at the CNPRC. The staff noted that the animal required auditory cues, such as gently taping on the cage bars and had to examine treats presented to him very closely prior to grasping them. He also appeared to exhibit social behavior suggesting difficulty reading social cues. When presented him with photographs of a male with a threat face or one with a female rump, which both trigger characteristics responses, the affected animal only reacted appropriately when the stimuli were presented at about 2 inches from his face, whereas most other animals reacted to the images from distances of several feet.

On clinical examination, the affected macaque had a myopic refractive error of −15.5 diopters (D) in the right eye and −11.5 D in the left eye by streak retinoscopy, and increased axial lengths of 21.01 mm in the right eye and 21.94 mm in the left eye on A-scan biometry, as compared to a cohort of 39 normal adult animals (age range = 3.9–28.3 years old, 64.10% female) evaluated at CNPRC which had a mean (SD) refractive error of 0.05 (4.21) D and axial length of 20.04 (1.16) mm (Fig. 1A). The axial elongation was primarily due to greater anterior and vitreous chamber depth rather than lens thickness (Fig. 1B). Intraocular pressures were within normal limits, and slit lamp examination revealed mild nuclear sclerotic cataracts but no other anterior segment abnormalities in both eyes (Fig. 1C).

Indirect ophthalmoscopy and fundus photography (FP) revealed prominent fundus tessellation and scattered regions of hypopigmentation in the macular region of both eyes (Fig. 1D). The retinal vascular pattern particularly in the right eye showed some distortion, but similar vascular findings were not identified among a cohort of 40 myopic rhesus macaques with axial length >21 mm (age 7.3–29.0 years old) that were examined as part of other ongoing studies at CNPRC. IR images did not show any evidence of retinal hemorrhage (Fig. 1E), and FA did not demonstrate dye leakage suggestive of choroidal neovascularization (Fig. 1F). Blue-peak fundus AF revealed some irregular areas of hypoautofluorescence and a few punctate spots of hyperautofluorescence, but neither revealed clear regions of chorioretinal or RPE atrophy which may occur in degenerative myopia (Fig. 1G). OCT imaging of the affected animal revealed ILM disruption and foveoschisis within primarily the OPL in both eyes, and a focal region of subretinal fluid in the right eye (Fig. 1H). The animal underwent necropsy at 14 months after the initial examination due to liver amyloidosis, at which time the schisis cavities had expanded in both eyes, and the foveal detachment increased in the right eye (Fig. 1I). The macular anatomy of this affected macaque contrasts with age-matched control animals with normal-appearing foveae (Fig. 1J), and shares some features seen in human patients with XLRS (Fig. 1K). However, the posterior bowing of the scleral wall and ILM disruption, in addition to the clinical myopia and axial elongation, are more consistent with myopic foveoschisis (Fig. 1L). To further explore the cellular and gene expression profile of this affected animal, we cryo-preserved the right eye for immunohistochemistry, and the left eye for single-nuclei transcriptomic analysis.

Retinal Glial and Photoreceptor Morphology in NHP Foveoschisis

Immunohistochemistry of macular and peripheral retina of the affected macaque revealed GFAP expression in astrocytes within the nerve fiber layer of the foveal region and peripheral areas (Figs. 2A–2C) similar to age-matched control animals with normal foveal anatomy (Figs. 2D–2F), but also increased GFAP+ Muller glia within the OPL, similar to those seen in *Rs1*-knockout mice and consistent with macroglial activation resulting from cellular stress. Additionally, Iba-1+ microglia in the animal with foveoschisis adopted more amoeboid morphology in the foveal region (see Figs. 2A, 2B) indicating microglial activation. By contrast, Iba-1+ cells in the peripheral retina of the affected animal (see Fig. 2C) showed a similar dendritic morphology as the mature, resting microglia seen in the foveal and peripheral retina of control animals (see Figs. 2D–2F). Due to the photoreceptor layer disruption at the fovea (see Fig. 2A), we examined rhodopsin+ rod and M/L opsin+ cone photoreceptors in the parafoveal macula and peripheral retina of the affected animal (Figs. 2G-2I), and found similar photoreceptor density to age-matched control animals (Figs. 2J-2L). Together, the increased GFAP expression in Muller glia and loss of ramified Iba-1+ microglia in the foveal region of this animal indicate macroglial and microglial activation in response to the mechanical traction, with relatively less disruption of rod or cone photoreceptor morphology outside of the foveal region of the macula.

Cellular and Gene Expression Profile in NHP Foveoschisis

We recovered 27,568 nuclei from the central macula of the affected macaque and performed snRNA-seq of the retinal tissue. For reference, we performed snRNA-seq on 7566 nuclei from the pooled maculae of three unrelated normal macaques. Using unsupervised clustering of gene expression profiles, we identified seven major transcriptionally distinct cell populations, including rod and cone photoreceptors, horizontal cells (HCs), bipolar cells (BCs), Müller glia (MG), amacrine cells (ACs), and retinal ganglion cells (RGCs), which were compared with those from the three pooled control samples (Fig. 3A). A majority of the nuclei were derived from rod photoreceptors and bipolar cells, with similar proportion of all retinal cell types between the affected and control animals (Fig. 3B). We then analyzed DEGs between affected and control tissues for each of the seven major retinal cell types ($P < 0.001$, fold change >2), and found most DEGs within RGCs and cone photoreceptors (Fig. 3C), likely due to the higher proportion of these cell types at the central macula. The top GO terms ($P < 0.001$) enriched by DEGs for each cell type included genes involved in chromatin and histone modifications, often associated with cellular stress, across cones, RGCs, and ACs, neurite development in BC, and phototransduction in rods, while none of the GO terms were statistically significant in HC and Müller glia (Fig. 3D, Supplementary Fig. S1).

Normal RS1 Gene and Expression in NHP Foveoschisis

RS1 is an extracellular retinal protein involved in maintaining retinal architecture, and is defective in XLRS.[6] To

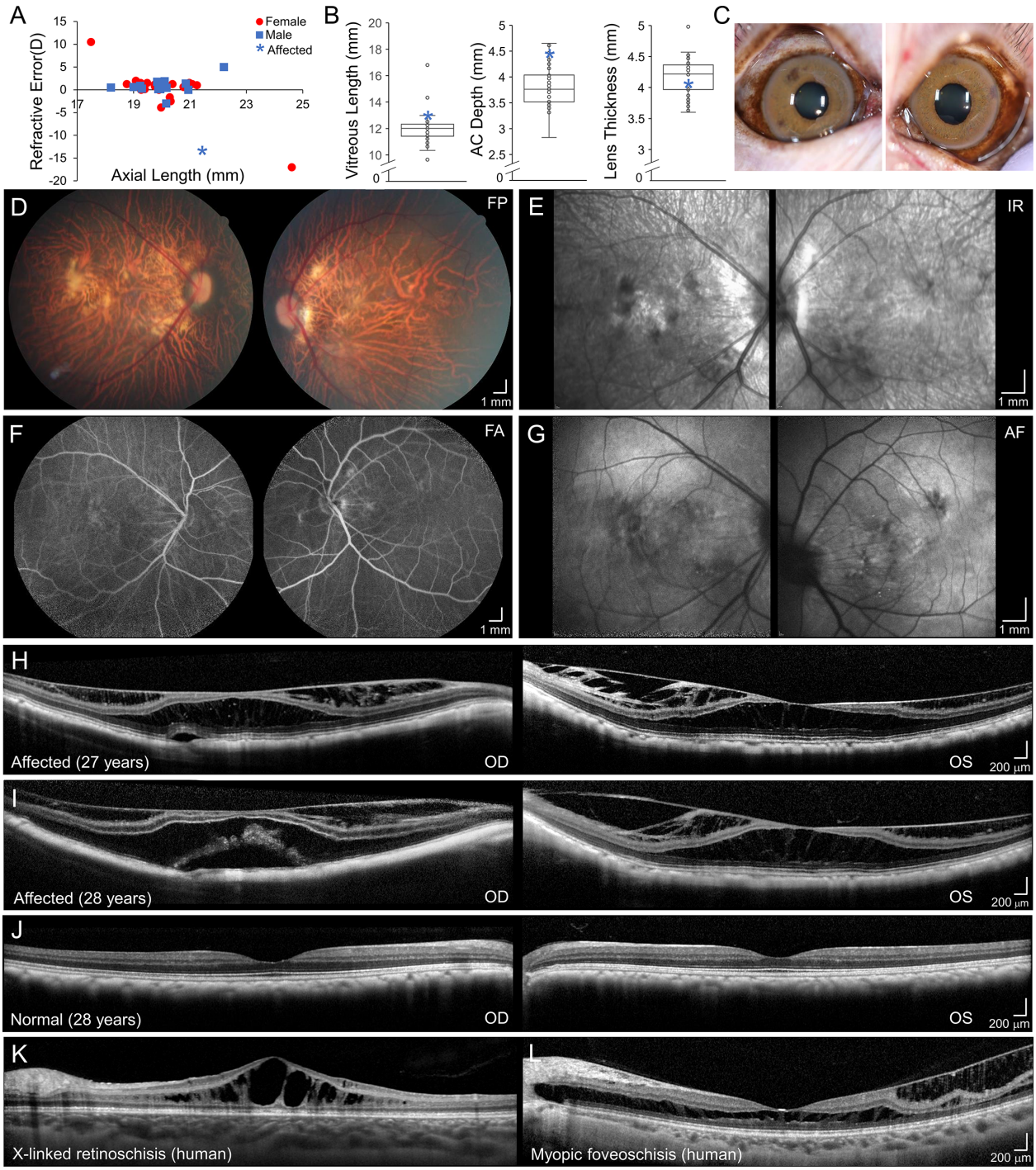

Figure 1. Clinical examination and multimodal imaging of NHP foveoschisis. (**A**) Scatterplots of refractive errors and axial lengths of adult rhesus macaques at the California National Primate Research Center that underwent streak retinoscopy and A-scan biometry, separated by sex, including the affected animal (*asterisk*). (**B**) Boxplots of average vitreous length, anterior chamber (AC) depth, and lens thickness comparing the affected animal (*asterisk*) to other adult macaques. (**C**) External photographs, (**D**) color fundus photographs (FP), (**E**) infrared reflective (IR), (**F**) late-phase fluorescein angiography (FA), (**G**) blue-peak fundus autofluorescence (AF), and (**H**) spectral-domain optical coherence tomography (OCT) imaging of left and right eyes of the affected macaque at presentation at 27 years of age, and (**I**) repeat OCT imaging of the same animal 14 months later at time of necropsy. For comparison, representative OCT images from (**J**) a normal age-matched macaque, (**K**) a 7-year-old boy with X-linked retinoschisis, and (**L**) a 23-year-old woman with -15-diopters pathologic myopia and myopic traction maculopathy. Abbreviations: OD, right eye; OS, left eye. Scale bars, 200 µm to 1 mm.

investigate the potential relationship between XLRS and the foveoschisis observed in our affected animal, we analyzed the RS1 gene at the DNA, RNA, and protein level. By Sanger sequencing, we detected five variants in the introns and 3′ untranslated region (UTR) of RS1, four of which were present only in the affected macaque and absent in the

Investigative Ophthalmology & Visual Science

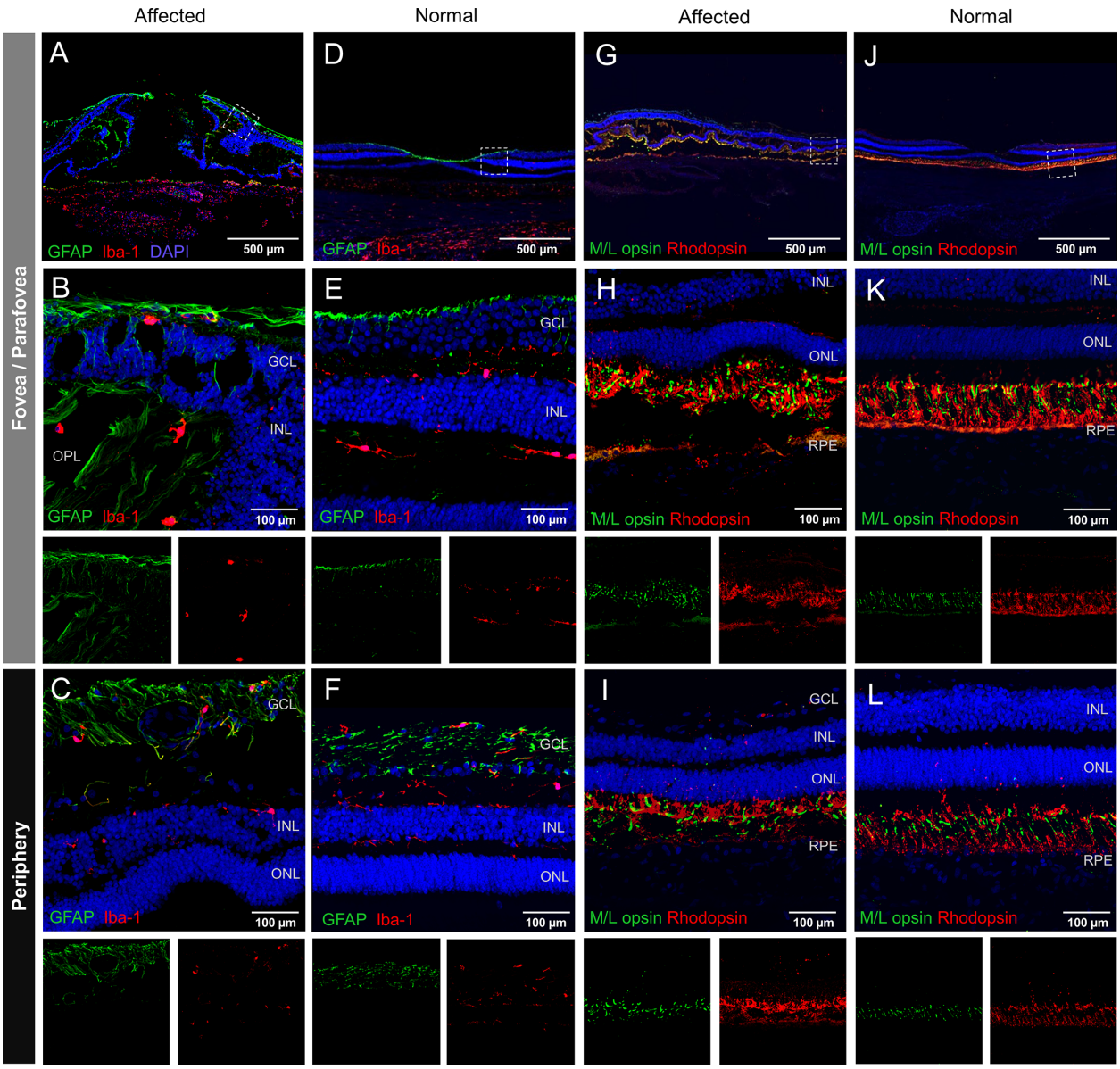

Figure 2. Retinal glial and photoreceptor morphology in NHP foveoschisis. Confocal fluorescence images of (**A–F**) glial fibrillar acidic protein (GFAP)-stained macroglia (*green*) and IBA-1+ microglia (*red*), or (**G–L**) rhodopsin+ rod (*red*) and M/L-opsin+ cone photoreceptors (*green*), along with DAPI (*blue*) to label cell nuclei, located at the foveal or parafoveal region **A**, **D**, **G**, and **J**, with magnified views of the dashed-box regions shown in **B**, **E**, **H**, and **K**, and peripheral retina **C**, **F**, **I**, and **L** in the rhesus macaque affected by foveoschisis **A** to **C** and **G** to **I** and representative age-matched control animal **D** to **F** and **J** to **L**. Abbreviations: GCL, ganglion cell layer; INL, inner nuclear layer; ONL, outer nuclear layer; and RPE, retinal pigment epithelium. Scale bars, 100 to 500 µm.

European Variation Archive (EVA) Release 3 for the rhesus rheMac10 genome (Fig. 4A), although none of these variants were present among the approximately 21,000 alleles in the gnomAD database (version 2.1.1), or were computationally predicted to impact gene splicing using SpiceAI. No defects were identified in the *RS1* gene coding region. Because none of the affected animal's relatives were alive at the time of diagnosis, potential phenotypic or genetic defects in family members could not be evaluated (Fig. 4B). Based on the snRNA-seq analysis, RS1 expression was primarily detected in rods and cones of the affected animal, and did not differ significantly from the three control animals (Fig. 4C). Immunohistochemistry using anti-RS1 antibody confirmed that RS1 protein was detectable mostly in the photoreceptor inner segments in both the fovea and periphery, similar to age-matched normal controls (Fig. 4D). Our findings suggest that the myopic foveoschisis in this NHP model does not exhibit any defect in the RS1 gene and expression, despite sharing phenotypic features of XLRS.

We finally performed whole exome sequencing (WES) on the affected animal and compared it with a reference database of 1046 rhesus macaque genomes with WES collected at various primate centers. We detected no variants in *RS1* in this animal, but identified four potentially deleterious alleles in Cadherin Related Family Member 1 (*CDHR1*), Death Domain-containing Protein 1 (*DTHD1*), and the retinoblastoma *RB1* gene (Supplementary Table S2). Specifically, two heterozygous alleles identified in *CDHR1*

Investigative Ophthalmology & Visual Science

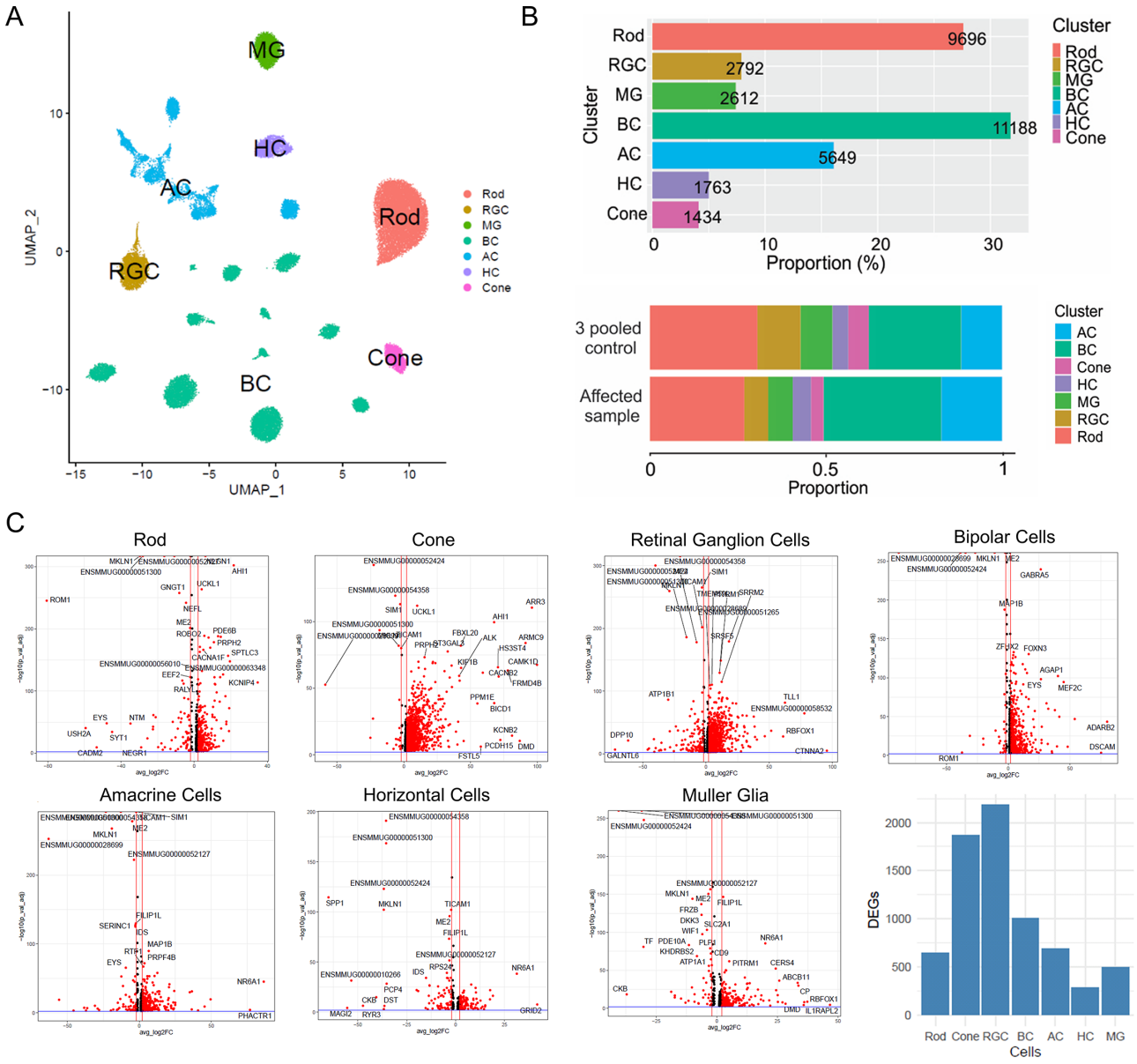

D

Cell Type	Top GO Term	Adjusted P-value
Cone	Covalent chromatin modification	6.94E-10
RGC	Covalent chromatin modification	3.10E-10
AC	Covalent chromatin modification	8.26E-10
BC	Regulation of neuron projection development	4.25E-10
Rod	Sensory perception of light stimulus	1.54E-07

Figure 3. Single-nuclei RNA sequencing analysis of retinal tissues in NHP foveoschisis. (**A**) Identified cluster of single-nuclei expression profiles from the affected rhesus macaque and three control macaque samples. (**B**) Bar graphs comparing distribution and proportion of the seven cell types in the foveoschisis animal compared to three controls. (**C**) Volcano plots demonstrating significant DEGs comparing the affected to control macaques (adjusted $P < 0.001$ and fold change >2) with a bar graph summarizing the total number of DEGs for each retinal cell types. (**D**) Top GO term enriched by each DEG lists from the identified retinal cell types. Abbreviations: ACs, amacrine cells; BCs, bipolar cells; HCs, horizontal cells; MG, Müller glia; and RGCs, retinal ganglion cells.

were predicted to be damaging, but one of them has a high allele frequency of 19.7% in the reference database, indicating that this variant may not be deleterious because *CDHR1* is an autosomal recessive disease gene and therefore is unlikely to be a causal gene. One homozygous allele identified in *DTHD1* has an allele frequency of 5.3%, but the deleteriousness prediction is weak. Finally, one heterozygous allele in *RB1* was predicted to be damaging and has an allele frequency of 0.33%, but the affected animal's phenotype is not consistent with that of patients with RB1 retinoblastoma. Further analyses revealed no significant causal WES variants associate with genes relating to

Investigative Ophthalmology & Visual Science

A

RS1 Variants	c.53-121C>G	c.78+92_c.78+93insGTTTGTTT	c.522+137C>T	c.*39C>T	c.327-151C>T
European Variation Archive R3	N/A	N/A	N/A	N/A	rs295830123
Affected Case	Present	Present	Present	Present	Present
Unaffected Control	Absent	Absent	Absent	Absent	Present
Human position (GRCh37/hg19)	X-18675906-G-C	insertion	X-18662427-G-A	X-18660085-G-A	X-18662896-G-A
Conservation	High	N/A	Low	Low	Low
gnomAD allele frequency	0/21k	0/21k	0/21k	0/21k	---
Splice prediction (splice AI; human)	No effect	N/A	No effect	N/A	---

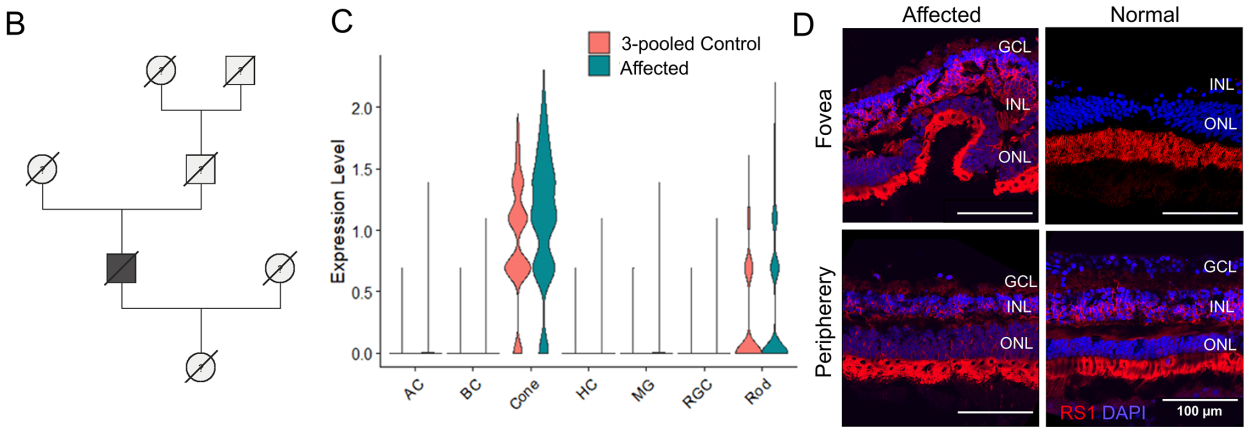

Figure 4. RS1 gene and expression in the retina of NHP with foveoschisis. (**A**) Table of gene variants identified in the introns and 3′ UTR of the *RS1* gene from the rhesus macaque with foveoschisis. (**B**) Pedigree showing the affected animal (*shaded*) with its relatives (*squares* = males, *circles* = females, *crossed lines* = deceased, and *question mark* = not examined). (**C**) Violin plots from snRNA-seq comparing RS1 expression in the affected macaque and 3 control animals showing RS1 expression mostly in rods and cones. (**D**) Confocal fluorescence images of the eye with foveoschisis and a 23-year-old control animal stained with antibodies against RS1 (*red*) and DAPI (*blue*) to label the nuclei. Abbreviations: GCL, ganglion cell layer; INL, inner nuclear layer; ONL, outer nuclear layer; RPE, retinal pigment epithelium. Scale bars, 100 µm.

other potentially similar inherited retinal disorders, such as familial exudative vitreoretinopathy (FEVR) or Stickler syndrome. Therefore, our extensive analysis suggests that the foveoschisis in the affected animal results from myopic traction rather than an inherited retinal disease.

Discussion

Animal models of macular diseases are rare because laboratory rodents, such as mice and rats, do not possess a cone-rich fovea. NHPs are the only mammalian species to possess a foveated macula resembling that in humans, and have successfully served as models of inherited and acquired macular degenerations. A naturally occurring mutation in the cone-specific phosphodiesterase 6c (*PDE6C*) gene and CRISPR-ablation of cyclic nucleotide-gated channel subunit beta 3 (*CNGB3*) have been described in rhesus macaques as spontaneous and induced NHP models of achromatopsia, respectively.[33,34] Drusen lesions characteristic of age-related macular degeneration (AMD) have also been discovered in Japanese and aged rhesus macaques.[35–37] In this study, we characterize a novel NHP model of foveoschisis by clinical examination, live imaging, and postmortem morphologic, cellular, and gene expression profiling of retinal tissues. We found that this macaque model exhibited phenotypic features of myopic foveoschisis caused by mechanical traction at the vitreomacular interface rather than genetic defects in *RS1*, with evidence of macroglial and microglial activation similar to XLRS but without significant photoreceptor degeneration. The transcriptional landscape of macular tissues in this foveoschisis model revealed alterations in gene expression, such as histone and chromatin modifications that are associated with cellular stress,[38] and were most pronounced in cones and RGCs (see Figs. 3C, 3D) likely due to the higher density of these cells at the central macula where the pathology manifests. Our results reveal similarities and differences between the cellular and molecular mechanisms underlying myopic and inherited forms of macular schisis.

Various lines of evidence support a myopic etiology over a genetic cause of the schisis observed in this model. First, the schisis cavities primarily affects the OPL as frequently observed in pathologic myopia,[39] rather than the inner nuclear layer (INL) which is more commonly affected in XLRS.[40] The schisis cavities also do not extend to the peripheral retina, which occurs in 50% of patients with XLRS. We identified no defects in the *RS1* gene sequence, transcript level, or protein expression as assessed by immunohistochemical (IHC) study, and retinal pathologies associated with candidate genes identified from WES are not consistent with the phenotype observed in this animal. We did not perform whole genome sequencing, as WES provides greater sequencing depth and a larger reference database of rhesus macaque WES data was available for comparison. Finally, the animal exhibited behavioral and clinical features of pathologic myopia. Ocular biometry confirmed axial ocular elongation approximately two standard deviations greater than the mean axial lengths from a cohort

Investigative Ophthalmology & Visual Science

of healthy eyes (see Fig. 1A) and normative values from published reports.[41,42] Because the animal had no living relatives at the time of evaluation, however, a more robust pedigree analysis could not be pursued. Identifying a myopic phenotype with a genetic association in NHPs would have been of incredible value.

In our model, we found increased GFAP expression within astrocytes and Müller glia at the central macula where the foveoschisis was most prominent and the foveal pit morphology was most severely disrupted. GFAP upregulation is a marker of cell stress and a well-characterized glial response to retinal injury.[43] We also found morphologic evidence of Iba1+ microglial activation, which also play prominent roles in the neuroinflammation seen in retinal degenerations.[44] Both macroglial and microglial activation have been reported in the RS1-/y mouse model of XLRS, and genetic rescue using AAV8-mediated RS1 gene transfer in these animals reverses the microglial-driven inflammatory state.[45,46] Interestingly, although Müller cells were initially postulated as the primary defect in XLRS due to the disproportionate impact on b-wave on ERG,[47,48] subsequent identification of the *RS1* gene and its protein expression supports photoreceptors and bipolar cells in the pathogenesis of this condition.[49–51] Because interactions between foveal cones and the ILM formed by Müller glia contribute to the formation and stabilization of the foveal pit,[52,53] we hypothesize that mechanical disruption of the foveal architecture in this myopic form of macular schisis leads to reactive glial responses similar to XLRS, but with relative sparing of photoreceptors. Although there are no IHC studies of human myopic foveoschisis published to date, surgical specimens of epiretinal membrane tissues removed from patients with myopic foveoschisis reveal glial and microglial cells in addition to hyalocytes,[54] consistent with our hypothesis.

The *RS1* gene product is an extracellular protein that associates with β2 laminin and αB-crystallin to stabilize extracellular matrix scaffolds,[55] as well as L-type voltage-gated calcium channels (LTCCs) involved in synaptic transmission.[56,57] RS1 is also anchored to plasma membranes by a retina-specific Na+/K+-ATPase, which appears to regulate cell survival through mitogen-activated protein kinase/extracellular signal-regulated kinase (MAPK/ERK) and calcium signaling that protects against apoptotic cell death.[58,59] In contrast to XLRS models, we observed no defects or deficiency in RS1 expression, which explains the preservation of photoreceptor integrity and survival in this animal. Thus, the glial responses we observed are more likely a consequence of mechanical traction and inner retinal disruption rather than the photoreceptor degeneration that mediates the pathogenesis of XLRS. Our study did not identify any other pathogenic variants on WES with known association with inherited retinal disorders. Several DEGs found on snRNA-seq are associated with retinal degenerations, including rod outer segment membrane protein 1 (*ROM1*, fold change = -80.65, adjusted *P* value = 4.95E-246) associated with retinitis pigmentosa and Abelson helper integration site 1 (*AHI1*, fold change = 67.64, adjusted *P* value = 3.42E-100) in Joubert syndrome. Future studies to validate the expression of these genes may help us better understand the impact of myopic foveoschisis on photoreceptor dysfunction.

Our results are limited by the single animal in this study, unknown duration of the pathology, and the inability to collect tissues at additional time points for analysis. We therefore could not evaluate gene expression as the anatomy worsened, when greater photoreceptor disruption may have occurred. Due to the rarity and sporadic nature of this model, as well as the high costs of NHPs, translational studies requiring more animals are not feasible. Nevertheless, animal modeling of macular diseases require species with a cone-rich macula, and additional screening of myopic macaques in primate colonies could help identify additional animals with myopic foveoschisis or similar macular disorders in future studies.

Acknowledgments

The authors thank Monica Motta for assistance with animal imaging, Mary Roberts and Paul-Michael Sosa for colony management, and John Morrison for CNPRC support.

Supported by the Office of Research Infrastructure Program/OD (P510D011107; CNPRC) and the large animal imaging core of NEI P30 EY12576. G.Y. is supported by NIH R01 EY032238, R21 EY031108, the BrightFocus Foundation, and Macula Society. S.T. and A.M. are supported by NIH U24 EY029904. No funding organizations had any role in the design or conduct of this research. The content is solely the responsibility of the authors and does not necessarily represent the official views of the funding agencies.

Disclosure: **T.-N. Sin**, None; **S. Kim**, None; **Y. Li**, None; **J. Wang**, None; **R. Chen**, None; **S.H. Chung**, None; **S. Kim**, None; **M.I. Casanova**, None; **S. Park**, None; **Z. Smit-McBride**, None; **N. Sun**, None; **O. Pomerantz**, None; **J.A. Roberts**, None; **B. Guan**, None; **R.B. Hufnagel**, None; **A. Moshiri**, None; **S.M. Thomasy**, None; **P.A. Sieving**, None; **G. Yiu**, Abbvie (C), Adverum (C), Alimera (C), Bausch & Lomb (C), Clearside (C), Endogena (C), Genentech (C), Gyroscope (C), Intergalactic (C), Iridex (C), Janssen (C), Myro (C), NGM Biopharmaceutical (C), Novartis (C), Regeneron (C), Thea (C), Topcon (C), Zeiss (C)

References

1. Wu PC, Chen YJ, Chen YH, et al. Factors associated with foveoschisis and foveal detachment without macular hole in high myopia. *Eye*. 2009;23(2):356–361.
2. George ND, Yates JR, Bradshaw K, Moore AT. Infantile presentation of X linked retinoschisis. *Br J Ophthalmol*. 1995;79(7):653–657.
3. Hahn LC, van Schooneveld MJ, Wesseling NL, et al. X-linked retinoschisis: novel clinical observations and genetic spectrum in 340 patients. *Ophthalmology*. 2022;129(2):191–202.
4. Rodríguez FJ, Rodríguez A, Mendoza-Londoño R, Tamayo ML. X-linked retinoschisis in three females from the same family: a phenotype–genotype correlation. *Retina*. 2005;25(1):69–74.
5. Georgiou M, Finocchio L, Fujinami K, et al. X-linked retinoschisis: deep phenotyping and genetic characterization. *Ophthalmology*. 2022;129(5):542–551.
6. Molday RS, Kellner U, Weber BHF. X-linked juvenile retinoschisis: Clinical diagnosis, genetic analysis, and molecular mechanisms. *Prog Retin Eye Res*. 2012;31(3):195–212.
7. Tolun G, Vijayasarathy C, Huang R, et al. Paired octamer rings of retinoschisin suggest a junctional model for cell–cell adhesion in the retina. *Proc Natl Acad Sci*. 2016;113(19):5287–5292.
8. Vijayasarathy C, Sardar Pasha SPB, Sieving PA. Of men and mice: human x-linked retinoschisis and fidelity in mouse modeling. *Prog Retin Eye Res*. 2022;87:100999.
9. Takano M, Kishi S. Foveal retinoschisis and retinal detachment in severely myopic eyes with posterior staphyloma. *Am J Ophthalmol*. 1999;128(4):472–476.

10. Gaucher D, Haouchine B, Tadayoni R, et al. Long-term follow-up of high myopic foveoschisis: natural course and surgical outcome. *Am J Ophthalmol*. 2007;143(3):455–462.e1.
11. Yiu G, Wang Z, Munevar C, et al. Comparison of Chorioretinal Layers in Rhesus Macaques using Spectral-Domain Optical Coherence Tomography and High-Resolution Histological Sections. *Exp Eye Res*. 2018;168:69–76.
12. Yiu G, Vuong VS, Oltjen S, et al. Effect of uveal melanocytes on choroidal morphology in rhesus macaques and humans on enhanced-depth imaging optical coherence tomography. *Invest Ophthalmol Vis Sci*. 2016;57(13):5764–5771.
13. Benhamou N, Massin P, Haouchine B, Erginay A, Gaudric A. Macular retinoschisis in highly myopic eyes. *Am J Ophthalmol*. 2002;133(6):794–800.
14. Sayanagi K, Morimoto Y, Ikuno Y, Tano Y. Spectral-domain optical coherence tomographic findings in myopic foveoschisis. *Retina*. 2010;30(4):623–628.
15. Sayanagi K, Ikuno Y, Soga K, Tano Y. Photoreceptor inner and outer segment defects in myopic foveoschisis. *Am J Ophthalmol*. 2008;145(5):902–908.e1.
16. Shimada N, Ohno-Matsui K, Baba T, Futagami S, Tokoro T, Mochizuki M. Natural course of macular retinoschisis in highly myopic eyes without macular hole or retinal detachment. *Am J Ophthalmol*. 2006;142(3):497–500.
17. Meng B, Zhao L, Yin Y, et al. Internal limiting membrane peeling and gas tamponade for myopic foveoschisis: a systematic review and meta-analysis. *BMC Ophthalmol*. 2017;17:166.
18. Ikuno Y, Sayanagi K, Soga K, Oshima Y, Ohji M, Tano Y. Foveal anatomical status and surgical results in vitrectomy for myopic foveoschisis. *Jpn J Ophthalmol*. 2008;52(4):269–276.
19. Morgan IG, Rose KA, Ashby RS. Animal models of experimental myopia: limitations and synergies with studies on human myopia. In: Spaide RF, Ohno-Matsui K, Yannuzzi LA, eds. *Pathologic Myopia*. New York, NY: Springer; 2014:39–58.
20. Zhong X, Ge J, Nie H, Chen X, Huang J, Liu N. Effects of photorefractive keratectomy-induced defocus on emmetropization of infant rhesus monkeys. *Invest Ophthalmol Vis Sci*. 2004;45(10):3806–3811.
21. Ostrin LA, Frishman LJ, Glasser A. Effects of pirenzepine on pupil size and accommodation in rhesus monkeys. *Invest Ophthalmol Vis Sci*. 2004;45(10):3620–3628.
22. Benavente-Perez A, Nour A, Troilo D. Short interruptions of imposed hyperopic defocus earlier in treatment are more effective at preventing myopia development. *Sci Rep*. 2019;9(1):11459.
23. Zeng Y, Qian H, Campos MM, Li Y, Vijayasarathy C, Sieving PA. Rs1h−/y exon 3-del rat model of X-linked retinoschisis with early onset and rapid phenotype is rescued by RS1 supplementation. *Gene Ther*. 2022;29(7):431–440.
24. Liang Q, Dharmat R, Owen L, et al. Single-nuclei RNA-seq on human retinal tissue provides improved transcriptome profiling. *Nat Commun*. 2019;10:5743.
25. Caskey JR, Wiseman RW, Karl JA, et al. MHC genotyping from rhesus macaque exome sequences. *Immunogenetics*. 2019;71(8-9):531–544.
26. Wang K, Li M, Hakonarson H. ANNOVAR: functional annotation of genetic variants from high-throughput sequencing data. *Nucleic Acids Res*. 2010;38(16):e164.
27. Liu X, Jian X, Boerwinkle E. Dbnsfp: a lightweight database of human nonsynonymous snps and their functional predictions. *Hum Mutat*. 2011;32(8):894–899.
28. Liu X, Wu C, Li C, Boerwinkle E. Dbnsfp v3.0: a one-stop database of functional predictions and annotations for human nonsynonymous and splice-site snvs. *Hum Mutat*. 2016;37(3):235–241.
29. Adzhubei I, Jordan DM, Sunyaev SR. Predicting functional effect of human missense mutations using PolyPhen-2. *Curr Protoc Hum Genet*. 2013;Chapter 7:Unit7.20.
30. Ioannidis NM, Rothstein JH, Pejaver V, et al. Revel: an ensemble method for predicting the pathogenicity of rare missense variants. *Am J Hum Genet*. 2016;99(4):877–885.
31. Kircher M, Witten DM, Jain P, O'Roak BJ, Cooper GM, Shendure J. A general framework for estimating the relative pathogenicity of human genetic variants. *Nat Genet*. 2014;46(3):310–315.
32. Kondo H. Complex genetics of familial exudative vitreoretinopathy and related pediatric retinal detachments. *Taiwan J Ophthalmol*. 2015;5(2):56–62.
33. Moshiri A, Chen R, Kim S, et al. A nonhuman primate model of inherited retinal disease. *J Clin Invest*. 129(2):863–874.
34. Lin Q, Lv JN, Wu KC, Zhang CJ, Liu Q, Jin ZB. Generation of nonhuman primate model of cone dysfunction through in situ aav-mediated cngb3 ablation. *Mol Ther Methods Clin Dev*. 2020;18:869–879.
35. Pennesi ME, Garg AK, Feng S, et al. Chapter 39 measuring cone density in a Japanese macaque (macaca fuscata) model of age-related macular degeneration with commercially available adaptive optics. *Adv Exp Med Biol*. 2014;801:309–316.
36. Yiu G, Tieu E, Munevar C, et al. In vivo multimodal imaging of drusenoid lesions in rhesus macaques. *Sci Rep*. 2017;7:15013.
37. Yiu G, Chung SH, Mollhoff IN, et al. Long-term Evolution and Remodeling of Soft Drusen in Rhesus Macaques. *Invest Ophthalmol Vis Sci*. 2020;61(2):32.
38. Johnson AB, Barton MC. Hypoxia-induced and stress-specific changes in chromatin structure and function. *Mutat Res*. 2007;618(1-2):149–162.
39. Gohil R, Sivaprasad S, Han LT, Mathew R, Kiousis G, Yang Y. Myopic foveoschisis: a clinical review. *Eye*. 2015;29(5):593–601.
40. Xiao Y, Liu X, Tang L, et al. X-Linked Retinoschisis: Phenotypic Variability in a Chinese Family. *Sci Rep*. 2016;6:20118.
41. Lin KH, Tran T, Kim S, et al. Age-related changes in the rhesus macaque eye. *Exp Eye Res*. 2021;212:108754.
42. Lin KH, Tran T, Kim S, et al. Advanced retinal imaging and ocular parameters of the rhesus macaque eye. *Transl Vis Sci Technol*. 2021;10(6):7.
43. Bringmann A, Iandiev I, Pannicke T, et al. Cellular signaling and factors involved in Müller cell gliosis: neuroprotective and detrimental effects. *Prog Retin Eye Res*. 2009;28(6):423–451.
44. Karlen SJ, Miller EB, Burns ME. Microglia activation and inflammation during the death of mammalian photoreceptors. *Annu Rev Vis Sci*. 2020;6(1):149–169.
45. Vijayasarathy C, Zeng Y, Brooks MJ, Fariss RN, Sieving PA. Genetic rescue of x-linked retinoschisis mouse (rs1−/y) retina induces quiescence of the retinal microglial inflammatory state following aav8-rs1 gene transfer and identifies gene networks underlying retinal recovery. *Hum Gene Ther*. 2021;32(13-14):667–681.
46. Gehrig A, Langmann T, Horling F, et al. Genome-wide expression profiling of the retinoschisin-deficient retina in early postnatal mouse development. *Invest Ophthalmol Vis Sci*. 2007;48(2):891–900.
47. Condon GP, Brownstein S, Wang NS, Kearns JA, Ewing CC. Congenital hereditary (juvenile x-linked) retinoschisis. histopathologic and ultrastructural findings in three eyes. *Arch Ophthalmol Chic Ill 1960*. 1986;104(4):576–583.

Investigative Ophthalmology & Visual Science

48. Gass JD. Müller cell cone, an overlooked part of the anatomy of the fovea centralis: hypotheses concerning its role in the pathogenesis of macular hole and foveomacualr retinoschisis. *Arch Ophthalmol Chic Ill 1960*. 1999;117(6):821–823.
49. Sauer CG, Gehrig A, Warneke-Wittstock R, et al. Positional cloning of the gene associated with X-linked juvenile retinoschisis. *Nat Genet*. 1997;17(2):164–170.
50. Grayson C, Reid SNM, Ellis JA, et al. Retinoschisin, the X-linked retinoschisis protein, is a secreted photoreceptor protein, and is expressed and released by Weri–Rb1 cells. *Hum Mol Genet*. 2000;9(12):1873–1879.
51. Molday LL, Hicks D, Sauer CG, Weber BHF, Molday RS. Expression of x-linked retinoschisis protein rs1 in photoreceptor and bipolar cells. *Invest Ophthalmol Vis Sci*. 2001;42(3):816–825.
52. Bringmann A, Unterlauft JD, Wiedemann R, Barth T, Rehak M, Wiedemann P. Two different populations of Müller cells stabilize the structure of the fovea: an optical coherence tomography study. *Int Ophthalmol*. 2020;40(11):2931–2948.
53. Delaunay K, Khamsy L, Kowalczuk L, et al. Glial cells of the human fovea. *Mol Vis*. 2020;26:235–245.
54. Vogt D, Stefanov S, Guenther SR, et al. Comparison of vitreomacular interface changes in myopic foveoschisis and idiopathic epiretinal membrane foveoschisis. *Am J Ophthalmol*. 2020;217:152–161.
55. Steiner-Champliaud MF, Sahel J, Hicks D. Retinoschisin forms a multi-molecular complex with extracellular matrix and cytoplasmic proteins: interactions with beta2 laminin and alphaB-crystallin. *Mol Vis*. 2006;12:892–901.
56. Morgans CW, Bayley PR, Oesch NW, Ren G, Akileswaran L, Taylor WR. Photoreceptor calcium channels: insight from night blindness. *Vis Neurosci*. 2005;22(5):561–568.
57. Shi L, Ko ML, Ko GYP. Retinoschisin facilitates the function of l-type voltage-gated calcium channels. *Front Cell Neurosci*. 2017;11:232.
58. Plössl K, Royer M, Bernklau S, et al. Retinoschisin is linked to retinal Na/K-ATPase signaling and localization. *Mol Biol Cell*. 2017;28(16):2178–2189.
59. Plössl K, Weber BHF, Friedrich U. The X-linked juvenile retinoschisis protein retinoschisin is a novel regulator of mitogen-activated protein kinase signalling and apoptosis in the retina. *J Cell Mol Med*. 2017;21(4):768–780.

Investigative Ophthalmology & Visual Science